Continuous-Flow Reactor Setup for *Operando* X-ray Absorption Spectroscopy of High Pressure Heterogeneous Liquid-Solid Catalytic Processes

Benedikt J. Deschner[1,a)], Dmitry E. Doronkin[2,3,a)], Thomas L. Sheppard[3,2], Georg Rabsch[1], Jan-Dierk Grunwaldt[3,2], Roland Dittmeyer[1,2]

[1]Institute for Micro Process Engineering, Karlsruhe Institute of Technology, Hermann-von-Helmholtz-Platz 1, Eggenstein-Leopoldshafen, 76344, Germany

[2]Institute of Catalysis Research and Technology, Karlsruhe Institute of Technology, Hermann-von-Helmholtz-Platz 1, Eggenstein-Leopoldshafen, 76344, Germany

[3]Institute for Chemical Technology and Polymer Chemistry, Karlsruhe Institute of Technology, Engesserstrasse 20, Karlsruhe, 76131, Germany

[a)]Authors to whom correspondence should be addressed: benedikt.deschner@kit.edu and dmitry.doronkin@kit.edu

KEYWORDS. heterogeneous catalysis, direct H_2O_2 synthesis, multiphase, *in situ*, packed bed, X-ray absorption spectroscopy.

ABSTRACT

A continuous-flow reactor and setup compatible with *operando* X-ray absorption spectroscopy (XAS) was designed for safely studying liquid-phase reactions on solid high atomic number transition metal catalysts (e.g., Au, Pd, Pt) under pressures up to 100 bar with temperatures up to 100°C. The reactor has a stainless-steel body, 2 mm thick polyether ether ketone (PEEK) X-ray windows, and a low internal volume of 0.31 mL. The rectangular chamber (6 x 5 x 1 mm^3) between the PEEK X-ray windows allows to perform XAS studies of packed beds or monoliths in transmission mode at any position in the cell over a length of 60 mm. A 146° wide-angle beam access also allows recording complementary X-ray fluorescence or X-ray diffraction signals. The setup was engineered to continuously feed a single-phase liquid flow saturated with one or more gaseous reactants to the liquid-solid XAS reactor containing no free gas phase, for enhanced process safety and sample homogeneity. The proof-of-concept for the continuous-flow XAS cell and high-pressure setup was provided by *operando* XAS measurements during direct synthesis of hydrogen peroxide at room temperature and 40 bar using 35 ± 5 mg catalyst (1 wt.-% Pd/TiO_2) and inline near-infrared (NIR) spectroscopy. The experiments prove that the system is well suited to follow the reaction in the liquid phase while recording high quality XAS data, paving the way for detailed studies on the catalyst structure and structure-activity relationships.

I. Introduction

Reactions with gaseous reactants or products over a solid catalyst in presence of a liquid phase are widely-used in industrial chemistry. These reactions are often performed at high pressures up to 100 bar and mild temperatures of 0–100 °C over supported metal catalysts in the presence of organic solvents. For example, selective hydrogenations of functional groups, are commonly performed at 1–10 bar H_2 partial pressure and 20–100°C, over Ni or noble metals (Pd, Pt, Ru) in the presence of aqueous or organic solvents [1,2]. Most catalytic hydrogenation reactions require both elevated H_2 pressures and liquid phase H_2 concentrations to proceed at a reasonable rate, especially if the active component is evenly distributed in the catalyst particle [1,3]. Therefore, H_2 partial pressures up to 100 bar at 25–65°C are also described in the literature for liquid-phase hydrogenations [4–6]. The need for gaseous reactants at high partial pressures also applies to other reactions, including selective oxidation. For example, selective oxidation of alcohols and aldehydes in organic and aqueous liquid solvents are commonly performed over noble metal (Au, Pd, Pt, Ru) catalysts using molecular O_2 [7,8].

A solid catalyst in contact with both gas and liquid (i.e., partially wetted catalyst) generally catalyzes reactions at the gas-solid interface as well as the liquid-solid interface [9,10]. Under high pressure but mild temperature, the liquid-phase species are commonly nonvolatile, i.e., less than 10% of liquid feed evaporates [9], so that purely liquid-solid processes are the focus of interest: (1) Feeding a single gaseous reactant and nonvolatile liquids, the nonwetted interior of the solid catalyst does not contribute to a reaction and lowers the catalyst efficiency [11,12]. Partial wetting of the catalyst exterior with liquid-filled pores, as found in trickle-bed reactors, is advantageous compared to full immersion due to lower external mass transport resistance [9,13–15]. (2) Feeding multiple gaseous reactants and nonvolatile liquids, the heterogeneously catalyzed gas phase

reactions are commonly detrimental to the catalyst stability or process safety. For example, dry supported palladium potentially ignites H_2/O_2 gas mixtures (oxyhydrogen reaction thermal runaway) but the same catalyst immersed in liquid forms hydrogen peroxide (targeted direct synthesis reaction). Heterogeneous liquid-solid catalytic processes, in particular on high atomic number transition metal catalysts under high pressure but mild temperatures, are therefore of great industrial relevance.

For economic and sustainable long-term operation, catalysts must be designed with high activity, selectivity, and stability as prerequisites. To reach this objective through rational catalyst design, knowledge of the underlying reaction mechanisms and structure-performance relationships of the working catalyst are essential [16]. X-ray absorption spectroscopy (XAS) is a powerful non-invasive characterization tool that provides detailed element-specific insights into the catalyst structure, such as local coordination environment and oxidation states for both amorphous and crystalline phases [17,18]. XAS is a bulk-averaging method, requiring good sample homogeneity in the cross section of the X-ray beam to obtain high-quality and representative data on the sample structure. The experimental challenge of *operando* XAS studies with a working catalyst therefore arises from the mutual consideration of two factors. Firstly, precise control of process conditions and therefore the chemical environment of the catalyst must be obtained, including mass transfer limitations which may arise at industrially relevant conditions[19]. Secondly, the sample environment must not impair the data quality of XAS acquisition at the synchrotron facility [19].

Specialized *in situ* flow cells have been developed to enable XAS studies in the field of heterogeneous catalysis, mostly for gas-phase reactions [18–22]. Sample environments for high-pressure and high-temperature catalytic reactions in dense fluids (liquid phase, supercritical fluids) are also known [23–27]. The latter are preferentially designed as continuous-flow reactors with

immobilized catalysts, allowing catalytic and XAS measurements in a closed system at the same time [28,29], with online analysis of reaction products (i.e., *operando* approach) [20]. Despite the high significance, *in situ* XAS reactors for high atomic number transition metal catalysts at mild temperatures but elevated pressure have hardly been addressed.

In this work, we fill the knowledge gap by describing an *in situ* XAS liquid-solid flow cell (Section II) and a continuous-flow setup to feed a single-phase liquid flow saturated with one or more gaseous reactants (Section III). The direct synthesis of H_2O_2 over a supported palladium catalyst in ethanol at 40 bar demonstrates the proof-of-concept of o*perando* XAS, and shows the limitations of packed beds in terms of mass transfer rate and pressure drop (Section IV).

II. Flow cell

X-ray windows – material and sealing

Appropriate materials for X-ray windows require chemical media compatibility, thermal and pressure resistance, as well as high X-ray transparency. From a technical perspective, beryllium is an ideal material for XAS studies at elevated pressures [30]. The low atomic number and density of beryllium leads to excellent X-ray transparency, strength-to-weight ratio, as well as heat transfer properties [30]. In contrast, care must be taken with beryllium windows to avoid exposure to the environment. Beryllium metal and compounds including BeO are classified as carcinogenic and toxic [31,32]. Hence, unless reaction conditions dictate otherwise, beryllium is generally avoided as a construction material and should be well protected from the environment if used.

Carbon-related materials (diamond [23,33], vitreous carbon [33,34]) and nitrides (BN [23], AlN [25]) are also commonly applied in high-pressure or high temperature XAS cells. All are hard, high-strength materials but they have a brittle nature. Their probability of failure increases with

the part dimensions and is subject to a statistical distribution [35–38]. Moreover, surface quality is important as only polished surfaces free from flaws result in maximum strength [33,35]. This is inconvenient for catalytic packed beds with hard catalysts and diluting materials (e.g., SiO_2, TiO_2, SiC) which can potentially scratch the windows, especially if no further protective foils or coatings are used. Safe dimensioning of X-ray windows with these materials is therefore not trivial.

Semi-crystalline high-performance thermoplastics built on light atoms (i.e., C, H, N, O) feature low volumetric X-ray absorption, furthermore allowing facile dimensioning through their elastic-plastic fracture mechanics. Two examples are polyether ether ketone (PEEK) and polyetherimide (PEI) which feature higher strength and temperature stability compared to standard engineering polymers (cf. Table S1). We consider PEEK as the preferred high-performance thermoplastic for XAS studies: it is highly resistant to ionizing radiation [39] and chemically compatible with most organic and inorganic chemicals including acids and bases, and (halogenated) hydrocarbons.

The performance of PEEK X-ray windows under elevated pressure and mild temperatures has already been demonstrated for stirred *in situ*/*operando* XAS gas-liquid-solid reactors [24,40] with different sealing concepts. Bayram et al. [40] constructed a low-volume stirred batch reactor from a commercial 9/16 in. stainless-steel tee fitting by replacing the stainless-steel compression ring and olive tube fitting with a custom-made PEEK blind plug serving as the X-ray windows. The low volume batch cell was employed in a catalytic hydrogenation XAS study at 50 bar H_2 and 100°C [40]. However, the sealing method of pressing PEEK between stainless steel is unfavorable for larger X-ray windows because it requires very high contact pressures to ensure tightness. Grunwaldt et al. [24] developed a 10 mL XAS batch reactor cell with a PEEK inset inserted into a stainless-steel body. The walls of the PEEK inset function as X-ray windows, enabling *operando* XAS studies up to 150°C. With additional beryllium reinforcement (0.5 mm thickness), *operando*

XAS could be performed at 250 bar and up to 250°C [24]. Polytetrafluoroethylene (PTFE) O-rings sealed the inlet flange [24] by its plastic deformation. The plasticity of PTFE is suitable for simple XAS flow cells in the low-pressure range. Recently, we developed a XAS flow cell using flat polycarbonate X-ray windows pressed onto a PTFE body for pressures up to 10 bar [41]. However, PTFE O-rings are difficult to insert into non-circular geometries because of their plasticity and stiffness. On the other hand, elastomer O-rings are widely available in a range of dimensions and material types. For this reason, we consider PEEK as an X-ray window in combination with an elastomeric O-ring as an optimal choice for *in situ*/*operando* XAS flow cells operating under high pressure and mild temperature.

Flow cell design

The continuous-flow XAS reactor presented in Figure 1a features a rectangular milled slit (60 mm × 5 mm × 1 mm, length × depth × width) to incorporate a rectangular-shaped catalyst packed bed. Alternative catalyst structures are feasible (e.g., monoliths, ceramic foams or 3D-printed catalytic static mixers [42,43]) provided that an access path for the X-ray beam is available. All individual parts are described in Table S2. The slit depth of 5 mm was chosen based on a total absorbance of approx. 2.0–2.5 for a 1 wt.-%Pd/TiO_2 catalyst around the Pd K edge and a Pd K edge jump of approx. 0.15. This allows XAS measurements in transmission geometry, which is the most common and effective acquisition mode in terms of signal quality and acquisition time [44]. The cell employs 2 mm thick PEEK plates as X-ray windows (Figure 2a). To prevent the catalyst being blown out under pressure, we incorporated screw-in sinter metal filters manufactured using electron-beam welding of a sinter metal filter onto a cannulated screw. The cannulated screws were obtained from commercially available screws (DIN 912 - M5 × 20) by

drilling out a hollow shaft and grinding off the cylinder head and part of the thread. These screw-in filters (Figure 2b) allow placing the connecting pipes very close to the frit itself to minimize dead volume. The cell volume between the screw-in filters is 0.31 mL. We note that any porous filter with a diameter of 4 mm can be used without electron beam welding with no impact on the function of the cell, although this may result in increased dead volume. These filters can be held in place (crimped) by correspondingly shortened cannulated screws. For reliable placement of the cell in the X-ray beam, tapped blind holes were included on one side of the cell (Figure 1b). The frame without stainless steel crossbars over the X-ray window allows XAS studies in transmission mode at any position over a maximum total length of 60 mm. We further aimed to obtain a frame height as low as possible. This also provides beam access over a wide angle (146°) to enable further X-ray studies with non-perpendicular X-ray beam geometry, e.g., for recording X-ray fluorescence or X-ray diffraction (Figure 3). The separately detachable frames allow also easy access to incorporate the sieved catalyst powder or other catalyst structure. The wetted parts of the cell, i.e., stainless steel, polyether ether ketone (PEEK) and fluoropolymer rubber gaskets, are compatible with a wide range of chemicals and thus for a variety of reactions.

A prerequisite for the collection of accurate data is that the concentrations in the measurement cell are not affected by leakage. Gaseous reactants permeate through PEEK and O-rings via the bulk solution-diffusion mechanism [45]. A simplified plug-flow model illustrates that permeation through the PEEK windows is negligible for flow rates higher than 0.001 mL/min (Supplementary Material, Section SI-3). A helium leak detector system (Pheonix, Leybold vacuum) confirmed a low experimental leakage rate of the flow cell below 10^{-8} mbar L s^{-1} which is below the usual acceptable leakage rates of 10^{-5}–10^{-3} mbar L s^{-1} [46]. Likewise, the reactor passed the pneumatic

pressure test procedure according to EN 13445-5 [47] for 100 bar nominal operation pressure (testing pressure 143 bar).

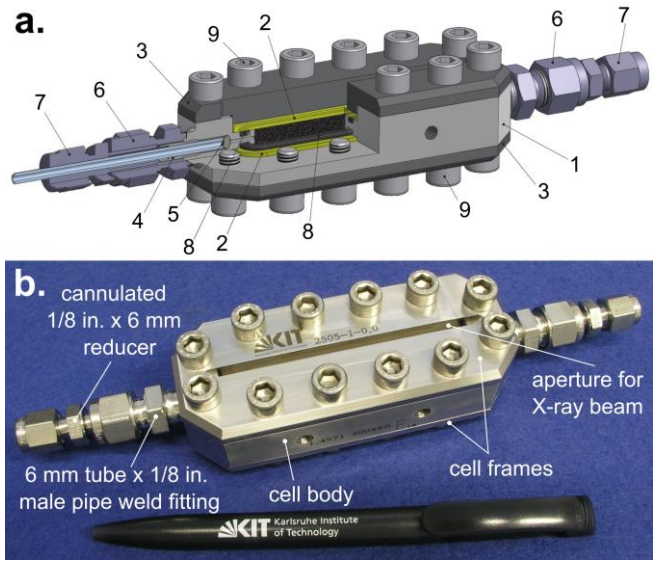

Figure 1: **(a)** Drawing of the assembled *in situ* continuous-flow XAS cell, numbers refer to list parts as described in Table S2. **(b)** Photograph of the manufactured cell.

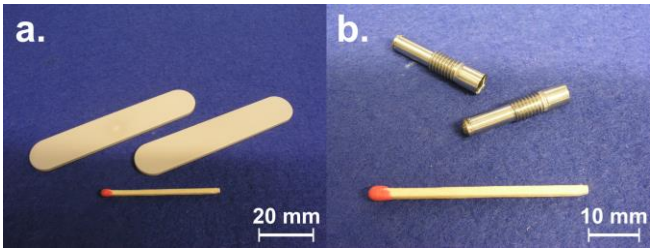

Figure 2: Detailed view of custom-made parts. **(a)** Milled PEEK windows and **(b)** screw-in inserts with electron beam-welded sinter metal filter.

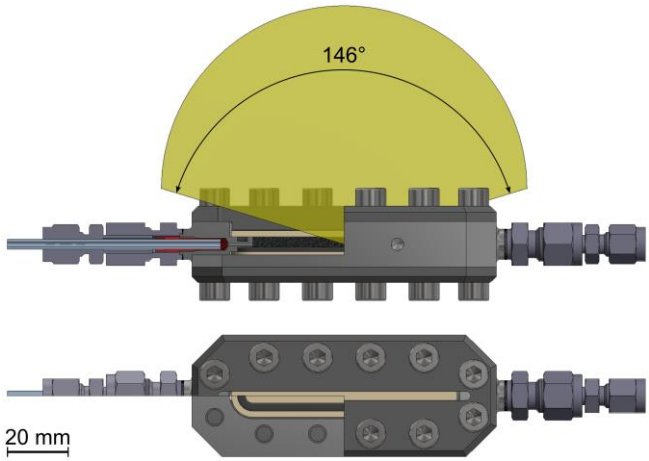

Figure 3: Accessibility of the outgoing X-ray beam over a wide angular range, allowing transmission, fluorescence and diffraction studies on the catalyst.

Maximum operating pressure of PEEK X-ray windows

We considered two failure mechanisms for the PEEK windows. Firstly, the maximum allowable stress of PEEK may be exceeded. Secondly, "gap extrusion" may cause O-ring scissure, i.e., extrusion of the elastomer in the clearance between PEEK plate and stainless-steel body (Figure S1). We calculated the stresses and deflections of the PEEK plate using finite element analysis (ANSYS® Mechanical™) on simplified quarter models of the flow cell, respectively (cf. Figure S2). To address the PEEK material failure, we compared the computed stress to the maximum allowable stress, a comparative value defined by the yield strength of PEEK (116 MPa, cf. Table S1) with a safety factor of 1.5 [48]. For a given plate thickness, the pressure was manually raised until either the maximum allowable stress or the maximum allowable gap for O-rings [49] exceeded the limits. Firstly, we studied the maximum operating pressure as a function of the X-ray windows thickness at 23°C, and secondly, we analyzed the temperature-dependent maximum operation pressure for 2 mm PEEK X-ray windows.

Above a plate thickness of 1 mm, deflection and gap size is the limiting factor at 23°C. Below 1 mm, the internal stress within the PEEK limits the maximum pressure (Figure 4). However, the strength of PEEK is strongly temperature-dependent: both yield strength and Young's modulus decrease linearly over a wide range between -50°C and 100°C and deteriorate as the glass-transition temperature at 143°C [50] is approached (cf. Figure S3a,b). We modeled material strength properties (yield stress, Young's modulus) with a stepwise linear behavior (25–125°C ; 125–140°C) with constant coefficients of linear thermal expansion for PEEK (47×10^{-6} K^{-1} [51]) and also stainless steel (17×10^{-6} K^{-1} [52]). The maximum allowable gap size determines the maximum operation pressure exceeding 200 bar for temperatures up to 75°C (Figure 5). The maximum operating pressure increases in this temperature range because of larger thermal expansion of PEEK compared to stainless steel, i.e., the thermal expansion compensates the pressure-driven clearance elongation. At higher temperature, the maximum operation pressure is determined by the stress and decreases rapidly (Figure 5). From a mechanical perspective, the design concept with 2 mm PEEK plates as X-ray windows is particularly suitable for a wide range of reactions for high pressures up to 100 bar with temperatures up to 100°C.

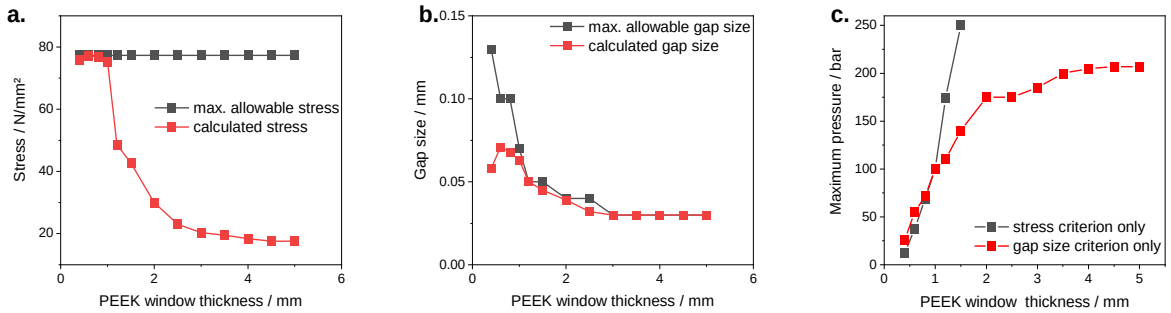

Figure 4: Design of the *in situ* continuous-flow cell against (a) maximal allowable PEEK stress and (b) O-ring extrusion at 23°C. **(c)** Maximal pressure as a function of PEEK window thickness at 23°C.

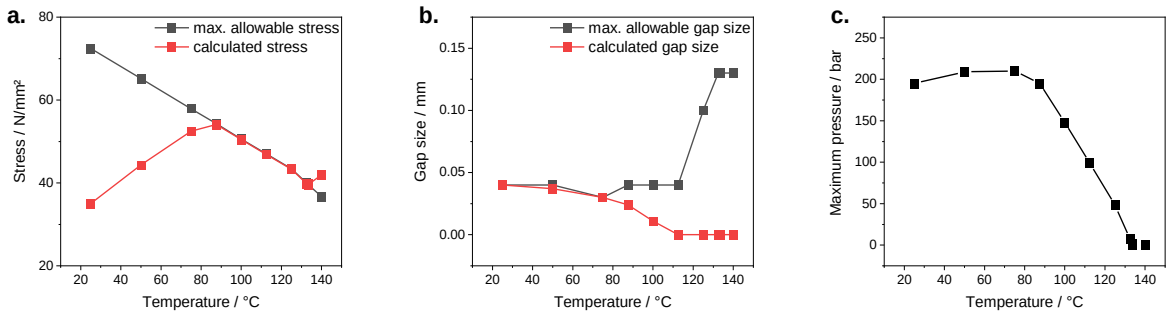

Figure 5: Design of the *in situ* continuous-flow cell with 2 mm PEEK X-ray windows against **(a)** maximal allowable PEEK stress and **(b)** O-ring extrusion. **(c)** Temperature dependence of overall maximum operation pressure with 2 mm PEEK X-ray windows using both stress and gap size criteria.

X-ray absorption of PEEK X-ray windows

For beamline layouts without mirrors for rejection of higher harmonics, the total attenuation coefficient of the sample and windows should not exceed 1.5. Our design in this environment is limited to energies above 20 keV (above Mo K edge) with light-atom support materials (e.g., C, SiO_2, Al_2O_3) but not with heavier transition metal oxides (e.g., TiO_2, CeO_2). Beamlines with high photon flux and mirrors for rejection of higher harmonics allow to measure samples with a total absorbance of 2.5–3.0. Provided the catalyst is supported on a light-atom material, our cell equipped with 2 mm PEEK windows allows XAS studies at the Pt L_3 (11.56 keV) and Au L_3 (11.92 keV) edges and – with thinner 1 mm windows – reaches as low as the Cu K edge (8.98

keV); see Figure 6. We note that the absorption of PEEK behaves very similarly to that of dense CO_2 [26]. Hence, the dense phase inside the cell substantially contributes to X-ray absorption at low X-ray energies (i.e., below 10 keV), requiring an overall short penetration path [26].

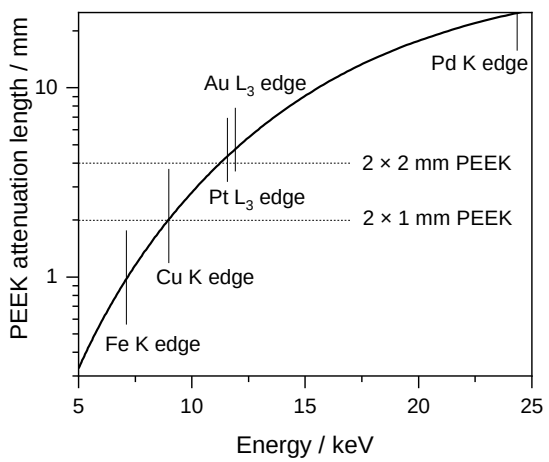

Figure 6: Attenuation length of PEEK at relevant energies around Fe K, Cu K, Pt L_3, Au L_3, and Pd K edges. Data obtained from ref. [53] using PEEK formula $C_{19}H_{12}O_3$ and density 1.32 g/mL according to ref. [54]. The attenuation length is the depth in the material, measured along the surface normal, at which the intensity of transmitted X-rays drops to 1/e (≈ 0.37) of its incident flux.

II. High pressure setup

Process design

Two different continuous experimental configurations are possible for solid-catalyzed liquid-phase reactions involving gases: (i) a three-phase gas-liquid-solid reactor, i.e., feeding both gas and liquid; (ii) a two-phase liquid-solid reactor feeding a single-phase liquid flow saturated with

one or more gaseous reactants upstream of the reactor. We consider the latter as a preferred configuration for *in situ*/*operando* XAS measurements, especially in packed bed reactors. Gas saturation upstream of the reactor (i.e., spatial separation of gas/liquid mass transfer and liquid/solid mass transfer) guarantees persistent wetting, which is a prerequisite for sample homogeneity. Experimental setups which take advantage of gas saturation upstream the reactor have already been presented for high-pressure hydroprocessing reactions with all hydrogen in the liquid phase [55,56]. In contrast, two-phase flow in a packed bed with particles smaller than 500 µm – also known as micro-packed bed (µPB) [57] – is a complex flow pattern influenced by interfacial tension which exhibits pronounced gas/liquid phase segregation [58]. Insufficient contact between the liquid phase and the catalyst may lead to drying. In the case of exothermic reactions (e.g., hydrogenations or the direct synthesis of hydrogen peroxide), this can provoke thermal runaway or ignition of the reaction mixture and represents a safety hazard. Moreover, feeding a bubble-free liquid allows to study reactions with gas mixtures in the explosive range, such as equimolar H_2/O_2 mixtures without inert gas dilution since no free gas phase is present in the reactor. These process advantages come at the price of higher system pressure: the spatial decoupling of liquid phase saturation and reaction limits the amount of gaseous reactant through its solubility in the liquid phase. This requires a high-pressure setup in order to effectively mimic industrially relevant process conditions.

High-pressure setup

We designed a continuous-flow test rig for operation pressures up to 100 bar and temperatures up to 204°C (limited by an optical transmission flow cell, *in situ* XAS cell temperature limit is lower as discussed earlier) based on many XAS studies of gas-liquid-solid XAS reactors and also

liquid-solid XAS reactors feeding liquids [28,59–65], see Figure 7. The test rig is constructed to dissolve two gases A and B in separate plant sections (referred to as “channels"), then mixing their bubble-free liquid-phase flows upstream of the *in situ* continuous-flow XAS reactor. Individual mass flow controllers (EL-FLOW Select®, Bronkhorst) and HPLC pumps (BlueShadow 40P, Knauer) directly control gas and liquid flowrates respectively, and operate independently of the system pressure. Hence, the liquid-phase molar concentration of the reactants is specified by the flows, provided that the system pressure is high enough for complete bubble-free gas dissolution. The HPLC pumps are equipped with an automatic pump-head flushing (isopropanol, ≥99.0%, VWR Chemicals). For continuous inline-saturation, gas and liquid reaction media are premixed in a side-tee mixing configuration upstream of the gas absorption columns (upstream concurrent flow). The columns were engineered from stainless steel pipes, 30 cm (length) × 1/2 in. (OD) packed with coarse silicon carbide (sieve fraction 150–200 µm, Alfa Aesar) for an enhanced mass transfer rate and reduced fluid holdup. The single-phase liquid streams exiting the gas absorbers are mixed in a regular tee piece. The feed passes either the *in situ* continuous-flow reaction cell containing the catalyst, or a transparent hose bypass, 1/16 in. (ID) × 1/8 in. (OD) × 40 cm (length) for visual confirmation of the gas dissolution level. Perfluoroalkoxy alkane (PFA) tubing (BOLA, burst pressure 140 bar, recommended maximal working pressure 35 bar) was chosen because of low gas permeability as well as good mechanical strength and chemical compatibility. Optical access by means of a transmission flow cell (3/8 in. Process Flow Cell, Ocean Optics) allows an inline and time-resolved assessment of the liquid-phase concentrations of the reactor effluent by ultraviolet–visible (UV-Vis) or near-infrared (NIR) spectroscopy. A dome-loaded backpressure valve (Research Line, Equilbar) controls the operating pressure which is displayed via a standard Bourdon-tube gauge (type 213.53, Wika). All pipes are made of stainless steel. Pipes before the

backpressure valve are sized 1/16 in. (ID) × 1/8 in. (OD), while tubing to the liquid product container is sized 1/32 in. (ID) × 1/16 in. (OD). Flexible stainless-steel hoses were used directly before and after the measurement cell to allow free positioning in the X-ray beam. A rotameter with a needle valve sets a flow of nitrogen (technical grade) to continuously flush the feed solution containers and the liquid product container, both of which are operated at atmospheric pressure. This secures a reproducible zero-point through a virtually oxygen-free atmosphere in the feed containers, as well as a non-flammable gas atmosphere below the lower flammability limit (LFL). The solvent and product containers are connected to the test rig via screw caps (size GL 45) with three threaded necks (size GL 14, equipped with tube fittings).

Safety note: Catalytic reactions with pressurized gas saturation upstream require special safety precautions because in many cases oxidizer (e.g., oxygen) and fuels (e.g., hydrogen, hydrocarbons) are mixed. Safety measures include exclusion of any electronic process measurement and control devices after mixing gases and liquids in the high-pressure part of the reactor, electrical grounding of the tubing, reactant gas high-flow mass flow controller shutdown, high-pressure pump shutdown, nitrogen purging of the containers, and small diameter tubes for minimized liquid holdup. The total fluid inventory of the high-pressure part of the experimental test rig is less than 50 mL.

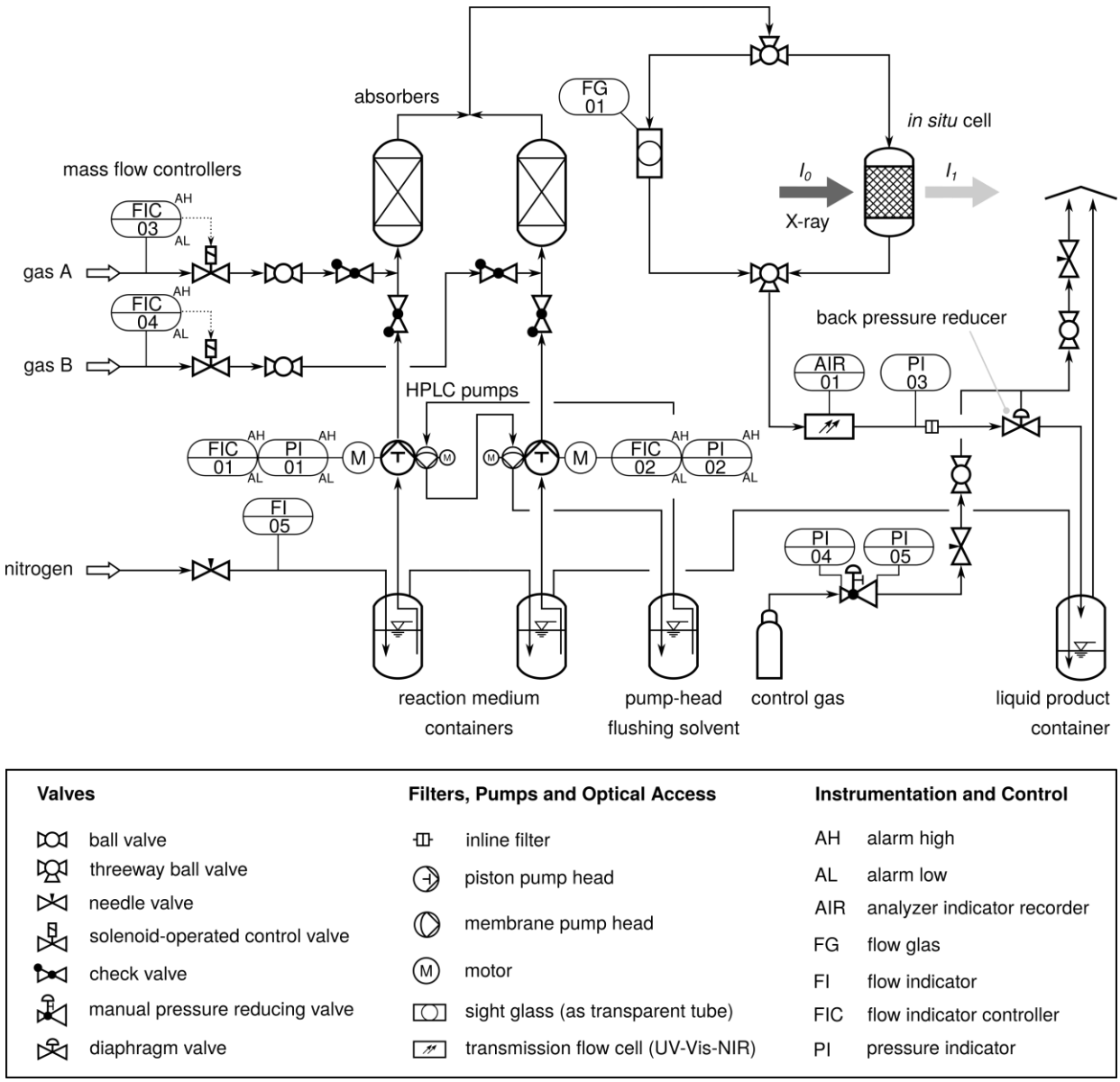

Figure 7: Detailed scheme of the process implementation of the high-pressure setup.

III. Proof of concept

Direct synthesis of hydrogen peroxide

The developed setup and the *in situ* continuous-flow cell were tested for direct synthesis of hydrogen peroxide (H_2O_2), which is an attractive but as yet uncommercialized green synthesis route for H_2O_2 synthesis, compared to the established industrial anthraquinone oxidation process

[66,67]. In this heterogeneously catalyzed reaction, molecular H_2 and O_2 are contacted over a palladium-based catalyst in the presence of a protogenic solvent (water, ethanol, methanol) [67,68]. The reaction is typically operated between 0–50°C and 1–50 bar [67,68] and is technically challenging since H_2 and O_2 form explosive gaseous mixtures over a wide range (4.0–95.2% H_2 in O_2 at atmospheric pressure [69]). In addition, high pressure is preferred due to the limited gas solubility of H_2 and O_2. Elevated reactant partial pressure therefore leads to higher hydrogen peroxide productivity [70].

Experimental procedure

A 1 wt.-% Pd/TiO_2 catalyst prepared by wet impregnation [41,71] was contacted in a single-phase liquid flow of absolute ethanol (≥ 99.8%, ACS, AnalaR NORMAPUR®, VWR BDH Chemicals) saturated with synthetic air (20.9 ± 0.2% O_2, 5.0 purity, Alphagaz™ 2, Air Liquide) and H_2 (5.0 purity, Alphagaz™ 1, Air Liquide) at 40 bar and room temperature. Prior to the reaction experiments, bubble-free saturation was verified via visual observation in the PFA bypass tubing with separate dosing of H_2 and synthetic air, respectively. We found experimentally that about 3.0 mL_{NTP}/min of pure H_2 dissolves in a flow of 1.0 mL/min ethanol, resulting in a H_2 concentration of 133.8 mmol/L at the outlet of the SiC gas absorber column of the H_2 channel. This is close to the thermodynamic limit at 40 bar (136.1 mmol/L at 298.2 K [72]). We were able to dissolve up to 28.70 mL/min of synthetic air (and thus 6.0 mL/min O_2) in 7.18 mL/min of ethanol in the O_2 channel. The synthetic air saturation is not thermodynamically controlled, but rather kinetically controlled. For both H_2 and O_2, no bubbles were visible for at least 45 minutes. We note that during this screening, the maximum operation pressure of the PFA tubing was purposefully exceeded by 5 bar. A 2.5 L volume product collection vessel was used because of the

high ethanol solution flow rate. The container was flushed with 300 mL/min N_2 to obtain nonexplosive conditions below the LFL.

The XAS flow cell was loaded with approx. 35 ± 5 mg catalyst (sieve fraction 50–200 µm), yielding a bed length of about 12 mm. The catalyst was packed between quartz wool, which in turn was packed between silicon carbide (sieve fraction 50–200 µm, Alfa Aesar). The purpose of SiC layers was to catch fine particles resulting from catalyst attrition which would otherwise clog the sintered metal filters, causing high pressure drop and ultimately flow blockage. This plugging method as opposed to pure glass wool was found to achieve a higher mechanical stability of the packed cell, thus reducing migration of the compact active catalyst zone. The plugging is achieved by opening the cell from one side and compacting the material in the direction of flow with a fine rigid wire or spatula. We note that the resulting bed porosity of 65% was higher than the typical value for a packed bed of monosized spheres (40%). The filling is not enclosed over the entire circumference (with respect to the compression axis), lowering the effective compressive forces in the bed. Furthermore, our particle collective was broadly distributed and not spherical.

Operando XAS measurements at the Pd K absorption edge were performed at the CAT-ACT beamline at the KIT synchrotron radiation source [73] using a 2.5 T wiggler source (40 poles, 48 mm period length) and a double crystal monochromator with a Si(311) crystal pair. The beam size was 0.6 mm (vertical) x 2 mm (horizontal), allowing the acquisition of XAS spectra at different positions in the catalyst bed, in particular the inlet and outlet zones. The experiments were performed in transmission geometry using ionization chambers (Figure 8). To test the catalyst at different H_2:O_2 ratios, the ethanol pump rates were kept constant (H_2 channel: 1.0 mL/min, O_2 channel: 7.18 mL/min) but different gas flows were set at the mass flow controllers within the allowed range (according to prior testing) of the high-pressure setup (Figure 9). Gas flows to obtain

the exemplified reference and reaction conditions were 1.0 mL_{NTP}/min H_2 , 1.0 mL_{NTP}/min H_2 and 4.8 mL_{NTP}/min synthetic air to yield a H_2:O_2 ratio of 1.0 (reactor feed: 16.4 mol/m^3), as well as 14.4 mL_{NTP}/min synthetic air for the O_2 condition (reactor feed: 49.4 mol/m^3). A fiberoptic NIR spectrometer (multispec® NIR, tec5) coupled to the high-pressure transmission cell monitored the absorbance of the reactor effluent between 905 and 2400 nm. Overtones of the O-H vibrations are accessible via NIR absorption, and thus the liquid phase concentration of H_2O_2 and H_2O; the latter is a by-product in the direct synthesis.

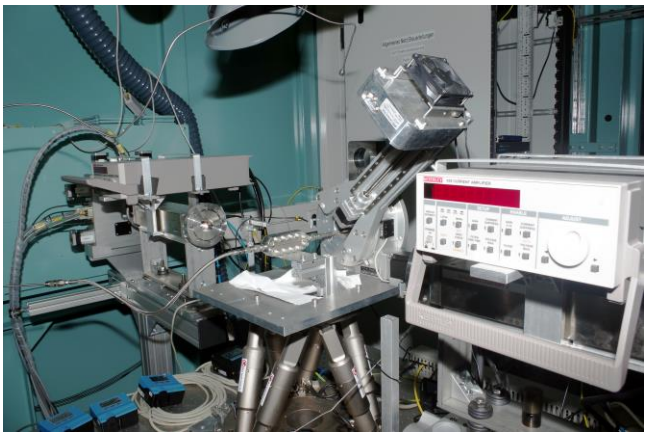

Figure 8: Side view of the X-ray transmission experiment with the flow cell attached to the hexapod for positioning and steel-jacketed tubing for connection to the reaction equipment.

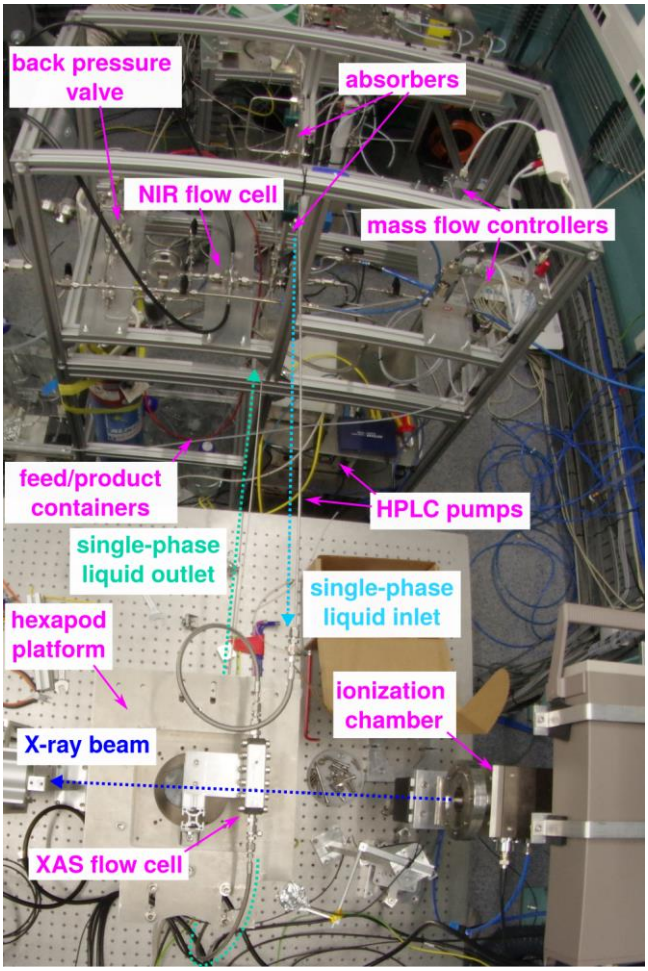

Figure 9: Top view of X-ray transmission experiment with high-pressure setup next to the X-ray experimental table.

Results

XAS spectra of the dry catalyst powder loaded in the flow cell (Figure 10) showed partially oxidized Pd species, similar to previous observations [41]. Introduction of the liquid flow did not result in higher noise or glitches in the EXAFS region (Figure 10b) highlighting good mechanical stability of the packed bed. At the same time, gradual reduction of Pd was observed which continued even after addition of O_2 to the flowing ethanol (O_2 was added at 2h 10 min after starting the liquid flow). The exemplary XAS spectra under H_2O_2 synthesis and reference conditions

(Figure 11) show only subtle but systematic changes with a switch from pure H_2 to pure O_2. The spectrum under working conditions with equimolar H_2:O_2 ratio shows features of palladium both in pure H_2 and pure O_2, respectively, indicating a good quality of the X-ray data. The strong absorbance peak at 1940 nm, a combination of the bending mode υ_2 and the asymmetric stretch mode υ_3 of the H_2O molecule (i.e., $\upsilon_2 + \upsilon_3$) [74], is prominent in the NIR spectrum and suitable for monitoring the reaction (Figure 12a). Following the absorbance at 1940 nm indicates that the catalyst and the concentration reached steady-state conditions after 2 h of time on stream (Figure 12b). We note that H_2O_2 can also be determined quantitatively in presence of water, e.g., applying partial least square (PLS) analysis of the first derivative at around 1500 nm or of the second derivative at around 1400 nm [75,76]. The O-H combination band [74] of H_2O_2 and H_2O is visible around 2060 nm as a shoulder of the 1940 nm peak (Figure S5).

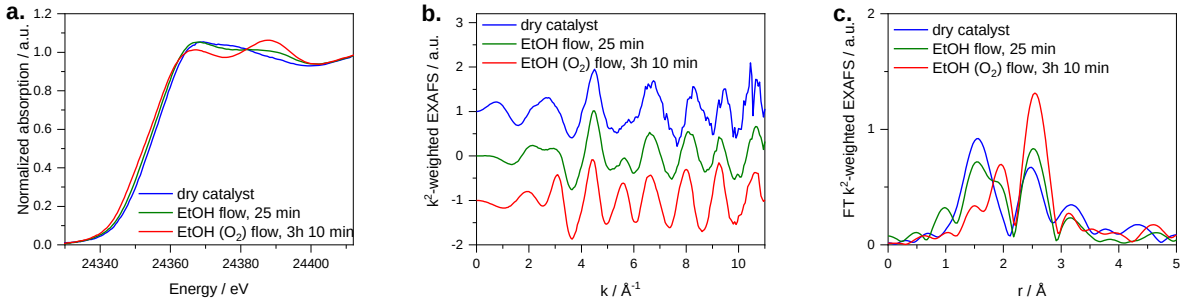

Figure 10: (a) Pd K edge XANES, **(b)** k^2-weighted EXAFS, and **(c)** Fourier-transformed k^2-weighted EXAFS spectra of the dry Pd/TiO_2 catalyst and the same catalyst in ethanol flow. Spectra are recorded near the end of the catalyst bed.

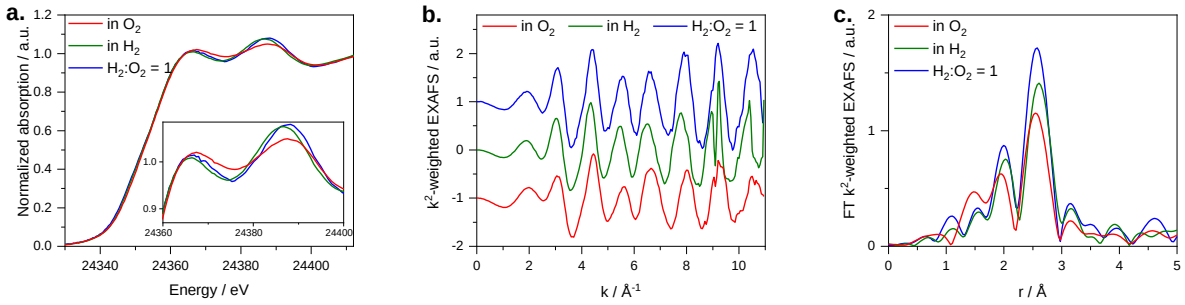

Figure 11: (a) Pd K edge XANES, **(b)** k^2-weighted EXAFS, and **(c)** Fourier-transformed k^2-weighted EXAFS spectra of the Pd/TiO_2 catalyst under reference conditions (H_2 and O_2 in ethanol) and stoichiometric H_2:O_2 ratio in ethanol. Spectra are recorded near the beginning of the catalyst bed.

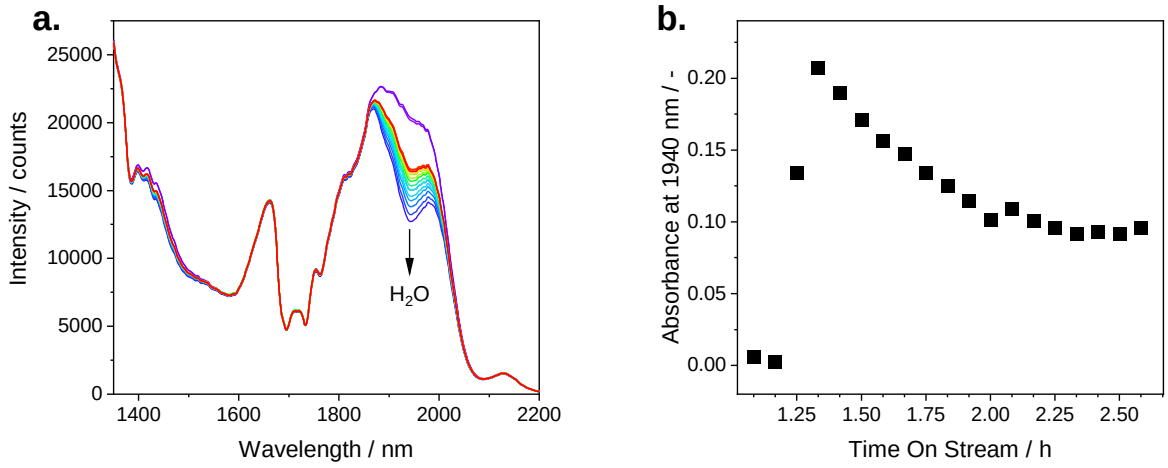

Figure 12: **(a)** Near-infrared absorbance spectrum of the reactor effluent and **(b)** corresponding temporal evolution of the absorbance at 1940 nm, recorded in transmission mode against N_2 (dry cell). Time on stream equal to zero corresponds to the moment of setting the fluid flow rates for H_2:O_2 = 1.

Discussion

Both XAS and NIR data prove that the developed setup and measurement cell enable *operando* XAS spectra of Pd catalysts with effective control of the reactant concentrations. Our flow cell design with an extended beam path of 5 mm ensures that sufficient catalyst particles are exposed to the X-ray beam so that the total penetrated sample thickness is relatively uniform. This avoids spatial inhomogeneities in the packed bed (e.g., pinholes) which can lead to inhomogeneous beam penetration [22] and decreased XAS spectral quality. Likewise, a catalyst sieve fraction of small particles improves sample homogeneity [22]. A fine catalyst powder is also advantageous in terms of external mass transfer and flow distribution. With smaller particles, higher liquid-solid mass transfer is obtained, and the plug-flow reactor criterion is reached [77]. However, finer particles can also result in higher pressure drop, which may cause catalyst migration and reactor blocking with time on stream. For a given catalyst particle system, the minimum tolerable particle size is limited and depends on particle shape, mechanical stability, and size distributions among other factors [78]. On the contrary, larger catalyst particles provoke internal mass transfer limitations. The selection of the particle size fraction is hence an important parameter for *operando* XAS studies in packed beds to balance the pressure drop of the packed bed as well as the external and the internal mass transport rates. Given the intrinsic reaction kinetics, the combination of the Weisz-Prater criterion, the Mears criterion, and the Ergun equation may be used to assess a suitable particle size fraction as outlined below. Details of the calculations are given in the Supplementary Material, Section SI-6 to SI-10.

For the chosen packing method of the 1 wt.-%Pd/TiO_2 catalyst, a sieve fraction between 50 and 200 µm was found to be suitable for flow rates up to 10 mL/min of ethanol solution, balancing pressure drop and flow distribution. Assuming the same behavior of 1 wt.-%Pd/TiO_2 in ethanol as

0.5% Pd/(1% C/Al_2O_3) in methanol [79] and typical values for the particle porosity and tortuosity ($\varepsilon = 0.50$, $\tau = 4$; $\rho_{Pd} \approx 20$ kg/m^3), the H_2O_2 synthesis experiments here were affected by internal mass transfer limitations. By feeding 16.4 mmol/L of both H_2 and O_2, the reaction is so fast ($-r_{O2}/c_{O2} \approx 1$ s^{-1}) that the effective reaction rate deviates by more than 5% from the intrinsic reaction rate with particles as small as 30 µm in diameter (Figure 13a,b). However, a packed bed of 30 µm spheres (40% bed porosity) causes a pressure drop above 3 bar per centimeter of packed bed length (Figure 13d) which triggers particle breakdown of the 1 wt.% Pd/TiO_2 catalyst. On the contrary, particles larger than 150 µm are affected by external mass transport limitations (Figure 13c). Note that a reduced amount of the active metal on the support and increased porosity may provide better catalyst utilization under the same harsh operating conditions. Compared to solvent-free cumene hydrogenation over a 14.4 wt.-%Ni/Al_2O_3 catalyst at 100°C, however, internal mass transfer limitations were found to be negligible for particles larger than 70 µm even at high H_2 concentration of 150 mol/m^3 (corresponding to 40 bar saturation pressure) [80], cf. Figure S6ab. Furthermore, external mass transport limitations in the packed bed were excluded for particles below 100 µm, which only cause 0.1 bar pressure drop per centimeter even at a high flow rate of 10 mL/min, cf. Figure S6cd.

These two reactions illustrate that the packed bed design is primarily suitable for *in situ/operando* XAS studies with moderate reaction rates. The rectangular geometry of our cell with appropriate X-ray windows and a wide-angle accessibility is also well suited for using structured catalysts, such as thin catalyst coatings for very fast reactions, but this was not yet addressed in the present study. The *in situ* continuous-flow XAS cell and high-pressure setup therefore constitute a versatile setup for *in situ/operando* XAS of catalytic reactions, paving the way to a better understanding of catalyst systems under industrially relevant conditions.

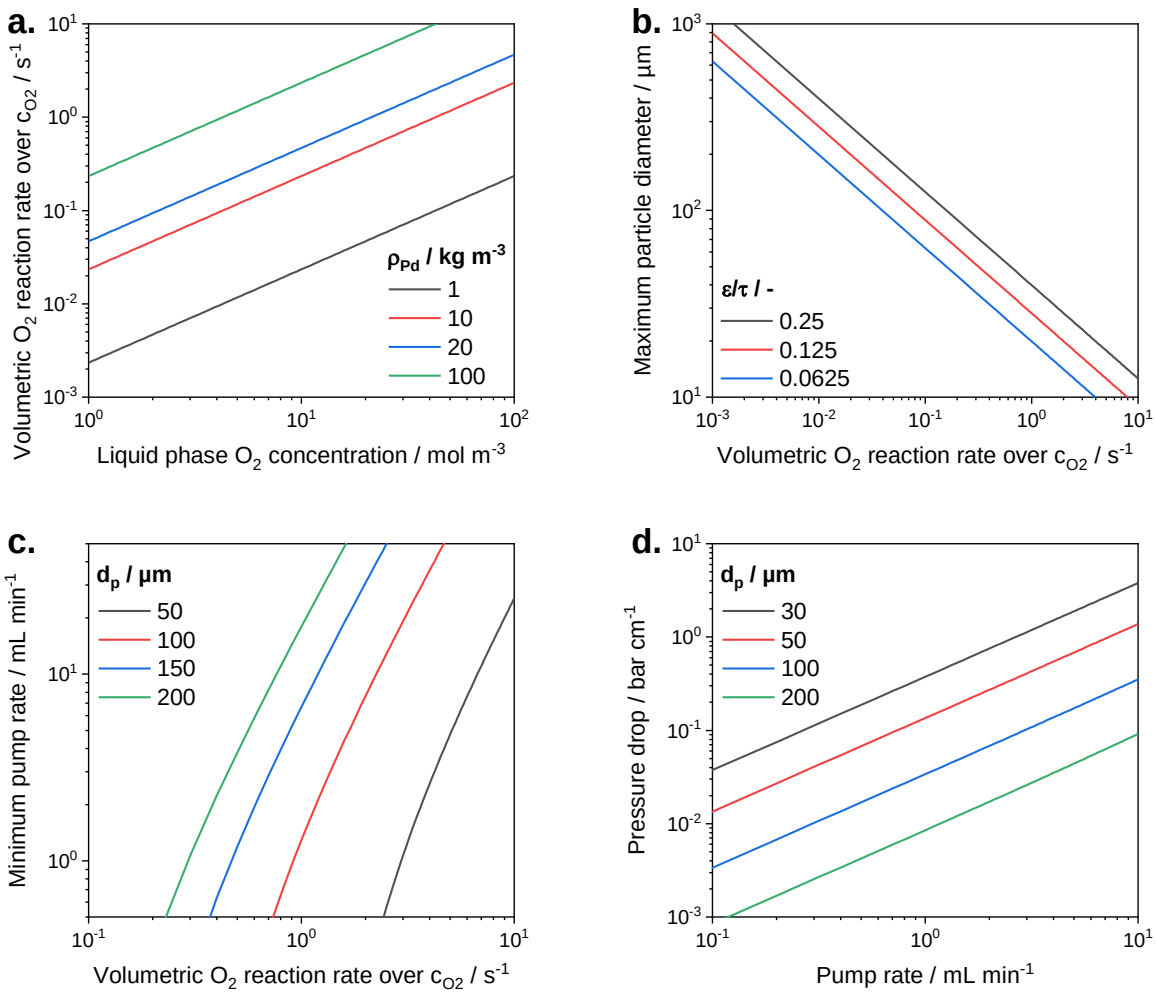

Figure 13: Experimental design considerations of the direct synthesis of H_2O_2 at 293.15 K in EtOH with H_2:O_2 = 1 and no H_2O_2 in the feed. **(a)** Intrinsic reaction rate according to ref. [79], **(b)** Weisz-Prater criterion for exclusion of internal mass transfer limitations with η = 95% effectiveness factor. **(c)** Mears criterion for exclusion of external mass transfer limitations and **(d)** pressure drop according to the Ergun equation.

IV. Conclusions

A versatile continuous-flow XAS reactor with gas and liquid dosing system are presented. The setup enables *operando* XAS measurements of liquid-phase reactions over solid high atomic number transition metal catalysts under pressures up to 100 bar and temperatures up to 100°C. We detail the design steps taken to ensure high-quality transmission XAS data without compromising the process engineering aspects, using the example of the direct H_2O_2 synthesis from molecular H_2 and O_2 as a challenging heterogeneously catalyzed reaction. The application of the relatively X-ray transparent thermoplastic PEEK as X-ray windows allows assisted design using finite element analysis. Moreover, within certain geometric constraints the XAS cell permits complementary fluorescence and diffraction measurements. The setup allows mixing of two liquid flows (each mixed with a gas stream) with easy variation of the liquid and/or gas ratios. Single-phase flow through the packed bed avoids distribution problems known in micro-packed beds. The catalytic activity can be monitored by inline optical (e.g., NIR or UV-Vis) spectroscopy but also combined with other online spectroscopic techniques. The functionality was demonstrated with data obtained on a typical Pd-based catalyst for direct H_2O_2 synthesis, and the limitations of packed beds regarding mass transfer and pressure drop were outlined. The application of the presented cell and dosing unit will offer new possibilities for better understanding the structure and mechanism of heterogeneously catalyzed reactions at mild temperatures but high pressures, such as selective oxidation or hydrogenation reactions.

SUPPLEMENTARY MATERIAL

The following files are available free of charge. SI-1, Properties of thermoplastics; SI-2, Part list of the flow cell; SI-3, Dimensioning of the PEEK X-ray windows; SI-4, Estimation of hydrogen permeation through PEEK X-ray windows; SI-5, Near-infrared (NIR) spectra of water and

hydrogen peroxide in ethanol; SI-6, Weisz-Prater criterion; SI-7, Mears criterion; SI-8, Ergun equation; SI-9, Kinetics of direct synthesis of hydrogen peroxide; SI-10, Kinetics of solvent-free cumene hydrogenation (PDF).

ACKNOWLEDGMENTS

We thank the Helmholtz Association for funding within the program Science and Technology of Nanosystems (STN). B.J.D. and R.D. acknowledge funding of this work by the German Research Foundation DFG through the Research Unit 2383 "ProMiSe" (www.promise.kit.edu) under grant numbers 694 Di 696/13-1 and Di 696/14-1. The authors declare no competing financial interest. We thank the IMVT and ITCP workshops at Karlsruhe Institute of Technology for their support. We would also like to thank the Institute for Beam Physics and Technology (IBPT) at Karlsruhe Institute of Technology for operation of the storage ring, the Karlsruhe Research Accelerator (KARA). We acknowledge the KIT light source for provision of instruments at the CAT-ACT beamline of the Institute of Catalysis Research and Technology (IKFT). We furthermore thank Dr. Anna Zimina and Dr. Tim Prüßmann for their help and technical support during synchrotron experiments.

NOMENCLATURE

EXAFS, extended X-ray absorption fine structure; ID, inside diameter; LFL, lower flammability limit; NIR, near-infrared; OD, outside diameter; PEEK, polyether ether ketone; PEI, polyetherimide; PFA, perfluoroalkoxy alkane; PLS, partial least squares; PTFE,

polytetrafluoroethylene; UV-Vis, ultraviolet–visible; XAS, X-ray absorption spectroscopy; XANES, X-ray absorption near-edge structure; μPB, micro-packed bed.

DATA AVAILABILTY

The data that support the findings of this study are available within the article and its supplementary material.

REFERENCES

1. H.-U. Blaser, A. Schnyder, H. Steiner, F. Rössler, and P. Baumeister, *Selective Hydrogenation of Functionalized Hydrocarbons* in *Handbook of Heterogeneous Catalysis*, edited by G. Ertl, H. Knözinger, F. Schüth, and J. Weitkamp (Wiley-VCH Verlag GmbH & Co. KGaA, Weinheim, Germany, 2008).
2. S. Nishimura, *Handbook of heterogeneous catalytic hydrogenation for organic synthesis* (Wiley, New York, Chichester, 2001).
3. V. G. Pangarkar, *Design of multiphase reactors* (Wiley-Blackwell, Chichester, 2015).
4. B. Desai and C. O. Kappe, J. Comb. Chem. **7**, 641 (2005).
5. G. Wang, R. Yao, H. Xin, Y. Guan, P. Wu, and X. Li, RSC Adv. **8**, 37243 (2018).
6. S. R. Konuspaev, K. N. Zhanbekov, N. V. Kul'Kova, and D. Y. Murzin, Chem. Eng. Technol. **20**, 144 (1997).
7. N. Dimitratos, J. A. Lopez-Sanchez, and G. J. Hutchings, *Supported Metal Nanoparticles in Liquid-Phase Oxidation Reactions* in *Handbook of advanced methods and processes in oxidation catalysis*. *From laboratory to industry*, edited by D. Duprez and F. Cavani (Imperial College Press, London, Singapore, 2014), p. 631.

8. H. P. L. Gemoets, Y. Su, M. Shang, V. Hessel, R. Luque, and T. Noël, Chem. Soc. Rev. **45**, 83 (2016).

9. M. P. Dudukovic, Ž. V. Kuzeljevic, and D. P. Combest, *Three-Phase Trickle-Bed Reactors* in *Ullmann's Encyclopedia of Industrial Chemistry* (Wiley-VCH Verlag GmbH & Co. KGaA, Weinheim, Germany, 2000).

10. G. Biardi and G. Baldi, Catal. Today **52**, 223 (1999).

11. E. G. Beaudry, M. P. Duduković, and P. L. Mills, AIChE J. **33**, 1435 (1987).

12. P. L. Mills and M. P. Duduković, Chem. Eng. Sci. **35**, 2267 (1980).

13. C. N. Satterfield, AIChE J. **21**, 209 (1975).

14. V. V. Ranade, R. V. Chaudhari, and P. R. Gunjal, *Trickle bed reactors*. *Reactor engineering & applications* (Elsevier, Amsterdam, 2011).

15. A. Azarpour, N. Rezaei, and S. Zendehboudi, J. Ind. Eng. Chem. **103**, 1 (2021).

16. J.-D. Grunwaldt, J. Phys.: Conf. Ser. **190**, 12151 (2009).

17. J. J. Rehr and R. C. Albers, Rev. Mod. Phys. **72**, 621 (2000).

18. B. M. Weckhuysen, Chem. Commun., 97 (2002).

19. S. D. Jacques, O. Leynaud, D. Strusevich, P. Stukas, P. Barnes, G. Sankar, M. Sheehy, M. G. O'Brien, A. Iglesias-Juez, and A. M. Beale, Catal. Today **145**, 204 (2009).

20. A. S. Hoffman, L. M. Debefve, A. Bendjeriou-Sedjerari, S. Ould-Chikh, S. R. Bare, J.-M. Basset, and B. C. Gates, Rev. Sci. Instrum. **87**, 73108 (2016).

21. J. S. Girardon, A. Y. Khodakov, M. Capron, S. Cristol, C. Dujardin, F. Dhainaut, S. Nikitenko, F. Meneau, W. Bras, and E. Payen, J. Synchrotron Radiat. **12**, 680 (2005).

22. J.-D. Grunwaldt, M. Caravati, S. Hannemann, and A. Baiker, Phys. Chem. Chem. Phys. **6**, 3037 (2004).

23. T. Kawai, W.-J. Chun, K. Asakura, Y. Koike, M. Nomura, K. K. Bando, S. Ted Oyama, and H. Sumiya, Rev. Sci. Instrum. **79**, 14101 (2008).

24. J.-D. Grunwaldt, M. Ramin, M. Rohr, A. Michailovski, G. R. Patzke, and A. Baiker, Rev. Sci. Instrum. **76**, 54104 (2005).

25. M. Dreher, E. de Boni, M. Nachtegaal, J. Wambach, and F. Vogel, Rev. Sci. Instrum. **83**, 54101 (2012).

26. J.-D. Grunwaldt and A. Baiker, Phys. Chem. Chem. Phys. **7**, 3526 (2005).

27. J.-D. Grunwaldt, R. Wandeler, and A. Baiker, Catalysis Reviews **45**, 1 (2003).

28. J.-D. Grunwaldt, C. Keresszegi, T. Mallat, and A. Baiker, J. Catal. **213**, 291 (2003).

29. D. E. Doronkin, H. Lichtenberg, and J.-D. Grunwaldt, *Cell Designs for In Situ and Operando Studies* in *XAFS techniques for catalysts, nanomaterials, and surfaces*, edited by Y. Iwasawa, K. Asakura, and M. Tada (Springer International Publishing, Cham, 2017), p. 75.

30. S. R. Bare, N. Yang, S. D. Kelly, G. E. Mickelson, and F. S. Modica, Catal. Today **126**, 18 (2007).

31. *Regulation (EC) No 1272/2008 of the European Parliament and of the Council of 16 December 2008 on classification, labelling and packaging of substances and mixtures, amending and repealing Directives 67/548/EEC and 1999/45/EC, and amending Regulation (EC) No 1907/2006* (2008).

32. United States Department of Labor, *OSHA Factsheet - Protecting Workers from Exposure to Beryllium and Beryllium Compounds: Final Rule Overview*, <https://www.osha.gov/Publications/OSHA3821.pdf>.

33. D. L. Graf, Phys. Rev. B **59**, 851 (1974).

34. V. F. Kispersky, A. J. Kropf, F. H. Ribeiro, and J. T. Miller, Phys. Chem. Chem. Phys. **14**, 2229 (2012).

35. D. C. Harris, *Materials for Infrared Windows and Domes: Properties and Performance* (SPIE Press, 1999).

36. A. A. Wereszczak, T. P. Kirkland, K. Breder, H.-T. Lin, and M. J. Andrews, Int. J. Microcircuits Electron. Packag. **22**, 446 (1999).

37. R. E. Bullock and J. L. Kaae, J. Mater. Sci. **14**, 920 (1979).

38. R. Spörl, *Einfluss des Gefüges auf mechanische Festigkeit und dielektrische Eigenschaften von CVD Diamant*. Doctoral thesis (2002), <https://dx.doi.org/10.5445/IR/672002>.

39. M. Talvet and H. van der Burgt, "Radiation resistance and other safety aspects of high-performance plastics by ERTA," in *International Workshop on Advanced Materials for High-precision Detectors*, edited by B. Nicquevert and C. Hauviller (CERN, Geneva, 1994), p. 157.

40. E. Bayram, J. C. Linehan, J. L. Fulton, J. A. S. Roberts, N. K. Szymczak, T. D. Smurthwaite, S. Özkar, M. Balasubramanian, and R. G. Finke, J. Am. Chem. Soc. **133**, 18889 (2011).

41. M. Selinsek, B. J. Deschner, D. E. Doronkin, T. L. Sheppard, J.-D. Grunwaldt, and R. Dittmeyer, ACS Catal. **8**, 2546 (2018).

42. M. Kundra, T. Grall, D. Ng, Z. Xie, and C. H. Hornung, Ind. Eng. Chem. Res. **60**, 1989 (2021).

43. L. L. Trinkies, A. Düll, B. J. Deschner, A. Stroh, M. Kraut, and R. Dittmeyer, Chem. Ing. Tech. **93**, 789-795 (2021).

44. D. Gianolio, *How to Start an XAS Experiment* in *X-Ray Absorption and X-Ray Emission Spectroscopy*, edited by J. A. van Bokhoven and C. Lamberti (John Wiley & Sons, Ltd, Chichester, UK, 2016), p. 99.

45. L. Monson, S. I. Moon, and C. W. Extrand, J. Appl. Polym. Sci. **127**, 1637 (2013).

46. K. Kutzke, *Dichtheitsprüfungen und Lecksuche mit dem Helium-Leckdetektor*. *Ein Leitfaden zum praktischen Einsatz bei der Qualitätssicherung und Wartung ; mit 3 Tabellen* (expert-Verl., Renningen-Malmsheim, 1998).

47. *DIN EN 13445-5:2018-12, Unfired pressure vessels, Part 5: Inspection and testing – German version* (Beuth Verlag, 2018).

48. Arbeitsgemeinschaft Druckbehälter, *AD-2000-Regelwerk*. *AD 2000 Regelwerk*, <http://swb.bsz-bw.de/DB=2.1/PPN?PPN=638418097>.

49. C. Otto Gehrckens GmbH & Co. KG, *O-Ring Basics*. *Everything about O-ring seals*, <https://www.cog.de/fileadmin/dokumente/Broschueren/COG_Broschuere_O-Ring_1x1_EN.pdf>.

50. P. J. Rae, E. N. Brown, and E. B. Orler, Polymer **48**, 598 (2007).

51. T. A. Osswald, E. Baur, S. Brinkmann, K. Oberbach, and E. Schmachtenberg, *Material Property Tables* in *International Plastics Handbook*, edited by T. A. Osswald, E. Baur, S. Brinkmann, K. Oberbach, and E. Schmachtenberg (Carl Hanser Verlag GmbH & Co. KG, München, 2006), p. 717.

52. F. Cardarelli, *Materials handbook. A concise desktop reference* (Springer, Cham, 2018).

53. Center for X-Ray Optics, *X-Ray Attenuation Length*, <https://henke.lbl.gov/optical_constants/atten2.html>.

54. A. K. van der Vegt and L. Govaert, *Polymeren*. *Van keten tot kunststof*, 5e dr (DUP Blue Print, Delft, 2003).

55. K. F. Eliezer, M. Bhinde, M. Houalla, D. Broderick, B. C. Gates, J. R. Katzer, and J. H. Olson, Ind. Eng. Chem. Fund. **16**, 380 (1977).

56. T. Nimmanwudipong, R. C. Runnebaum, K. Brodwater, J. Heelan, D. E. Block, and B. C. Gates, Energy Fuels **28**, 1090 (2014).

57. J. Zhang, A. R. Teixeira, L. T. Kögl, L. Yang, and K. F. Jensen, AIChE J. **63**, 4694 (2017).

58. N. Márquez, J. A. Moulijn, M. Makkee, M. T. Kreutzer, and P. Castaño, React. Chem. Eng. **4**, 838 (2019).

59. S. Urban, A. Weltin, H. Flamm, J. Kieninger, B. J. Deschner, M. Kraut, R. Dittmeyer, and G. A. Urban, Sens. Actuators, B **273**, 973 (2018).

60. P. Centomo, C. Meneghini, and M. Zecca, Rev. Sci. Instrum. **84**, 54102 (2013).

61. P. Centomo, C. Meneghini, S. Sterchele, A. Trapananti, G. Aquilanti, and M. Zecca, ChemCatChem **7**, 3712 (2015).

62. P. Centomo, C. Meneghini, S. Sterchele, A. Trapananti, G. Aquilanti, and M. Zecca, Catal. Today **248**, 138 (2015).

63. S. Kanungo, L. van Haandel, E. J. Hensen, J. C. Schouten, and M. F. Neira d'Angelo, J. Catal. **370**, 200 (2019).

64. C. Keresszegi, J.-D. Grunwaldt, T. Mallat, and A. Baiker, J. Catal. **222**, 268 (2004).

65. J.-D. Grunwaldt, M. Caravati, and A. Baiker, J. Phys. Chem. B **110**, 25586 (2006).

66. R. Dittmeyer, J.-D. Grunwaldt, and A. Pashkova, Catal. Today **248**, 149 (2015).

67. R. J. Lewis and G. J. Hutchings, ChemCatChem **11**, 298 (2019).

68. F. Menegazzo, M. Signoretto, E. Ghedini, and G. Strukul, Catalysts **9**, 251 (2019).

69. V. Schröder, B. Emonts, H. Janßen, and H.-P. Schulze, Chem. Eng. Technol. **27**, 847 (2004).

70. I. Huerta, P. Biasi, J. García-Serna, M. J. Cocero, J.-P. Mikkola, and T. Salmi, Green Chem. Process. Synth. **5**, 56 (2016).

71. T. Inoue, M. A. Schmidt, and K. F. Jensen, Ind. Eng. Chem. Res. **46**, 1153 (2007).

72. P. Luehring and A. Schumpe, J. Chem. Eng. Data **34**, 250 (1989).

73. A. Zimina, K. Dardenne, M. A. Denecke, D. E. Doronkin, E. Huttel, H. Lichtenberg, S. Mangold, T. Pruessmann, J. Rothe, T. Spangenberg, R. Steininger, T. Vitova, H. Geckeis, and J.-D. Grunwaldt, Rev. Sci. Instrum. **88**, 113113 (2017).

74. J. Workman and L. Weyer, *Practical guide and spectral atlas for interpretive near-infrared spectroscopy* (CRC Press, Boca Raton, FL, 2012).

75. Y.-A. Woo, H.-R. Lim, H.-J. Kim, and H. Chung, J. Pharm. Biomed. Anal. **33**, 1049 (2003).

76. A. M. Pimenta, S. H. F. Scafi, C. Pasquini, I. M. Raimundo, J. J. Rohwedder, M. C. B. Da Montenegro, and A. N. Araújo, J. Near Infrared Spectrosc. **11**, 49 (2003).

77. A. G. Dixon, Can. J. Chem. Eng. **66**, 705 (1988).

78. D. Wu, L. Song, B. Zhang, and Y. Li, Chem. Eng. Sci. **58**, 3995 (2003).

79. A. Pashkova, R. Dittmeyer, and H. Richter, *Schlussbericht AiF-Vorhaben Nr. 14782 BG/1 - Entwicklung eines inhärent sicheren, kostengünstigen und flexiblen Verfahrens zur Herstellung von Wasserstoffperoxidlösungen durch Direktsynthese mittels katalytisch beschichteter Membranen, 2009*, <https://dechema-dfi.de/kwi_media/Downloads/tc/Abgeschlossene+Projekte/2009+Direktsynthese+von+Wasserstoffperoxid+F487_Pashkova/Abschlussbericht_F487-p-1333.pdf>.

80. S. Toppinen, T.-K. Rantakylä, T. Salmi, and J. Aittamaa, Ind. Eng. Chem. Res. **35**, 1824 (1996).